

REPORT DOCUMENTATION PAGE				Form Approved OMB No. 0704-0188	
The public reporting burden for this collection of information is estimated to average 1 hour per response, including the time for reviewing instructions, searching existing data sources, gathering and maintaining the data needed, and completing and reviewing the collection of information. Send comments regarding this burden estimate or any other aspect of this collection of information, including suggestions for reducing the burden, to Department of Defense, Washington Headquarters Services, Directorate for Information Operations and Reports (0704-0188), 1215 Jefferson Davis Highway, Suite 1204, Arlington, VA 22202-4302. Respondents should be aware that notwithstanding any other provision of law, no person shall be subject to any penalty for failing to comply with a collection of information if it does not display a currently valid OMB control number.					
1. REPORT DATE (DD-MM-YYYY) 10-07-2008		2. REPORT TYPE Final Technical		3. DATES COVERED (From - To) 01/06/07-03/31/08	
4. TITLE AND SUBTITLE Oxide films for RF applications				5a. CONTRACT NUMBER	
				5b. GRANT NUMBER N00014-07-1-0503	
				5c. PROGRAM ELEMENT NUMBER	
6. AUTHOR(S) M. Skowronski				5d. PROJECT NUMBER	
				5e. TASK NUMBER	
				5f. WORK UNIT NUMBER	
7. PERFORMING ORGANIZATION NAME(S) AND ADDRESS(ES) Carnegie Mellon University, Office of Sponsored Research, 5000 Forbes Avenue, Pittsburgh, PA 15213				8. PERFORMING ORGANIZATION REPORT NUMBER	
9. SPONSORING/MONITORING AGENCY NAME(S) AND ADDRESS(ES) Office of Naval Research Chicago Regional Office 230 South Dearborn Avenue, Room 380 Chicago, IL 60604-1595				10. SPONSOR/MONITOR'S ACRONYM(S) ONR	
				11. SPONSOR/MONITOR'S REPORT NUMBER(S)	
12. DISTRIBUTION/AVAILABILITY STATEMENT					
13. SUPPLEMENTARY NOTES					
14. ABSTRACT <p>Several types of oxide superlattice structures were grown by MBE method and characterized by x-ray diffraction and TEM. $\text{Sr}_{m-1}\text{TiO}_{2+m}$ ($m=2,3,4$, and 5) phases having one TiO_2 layer sandwiched between m SrO layers were grown using molecular beam epitaxy. X-ray diffraction and electron microscopy confirmed the artificially layered structures. Locally nonstoichiometric superlattices $(\text{SrO})_m(\text{TiO}_2)_m$ (m from 2 to 33) inter-reacted during growth to form highly-crystalline epitaxial SrTiO_3. The relaxation of $\text{Ba}_{0.6}\text{Sr}_{0.4}\text{TiO}_3$ films grown on $\text{SrTiO}_3(111)$ substrates by pulsed laser deposition method was studied using transmission electron microscopy. It was observed that misfit dislocations form a triangular network in $[111]$-oriented films with dislocation lines in $\langle 11-2 \rangle$ directions and the Burgers vector are of $a\langle 1-10 \rangle$ type. This observation is not consistent with the accepted slip system $\langle 100 \rangle \{010\}$. Instead, we proposed that $\langle 110 \rangle \{1-10\}$ slip system is active in heteroepitaxy in the studied material system.</p>					
15. SUBJECT TERMS strontium titanate, barium titanate, molecular beam epitaxy, superlattice					
16. SECURITY CLASSIFICATION OF:			17. LIMITATION OF ABSTRACT SAR	18. NUMBER OF PAGES 1	19a. NAME OF RESPONSIBLE PERSON Marek Skowronski
a. REPORT U	b. ABSTRACT U	c. THIS PAGE U			19b. TELEPHONE NUMBER (Include area code) (412) 268-2710

20080721 204



DEFENSE TECHNICAL INFORMATION CENTER

Information for the Defense Community

DTIC[®] has determined on

Month	Day	Year
18	20	2008

 that this Technical Document has the Distribution Statement checked below. The current distribution for this document can be found in the DTIC[®] Technical Report Database.

☒ **DISTRIBUTION STATEMENT A.** Approved for public release; distribution is unlimited.

☐ **© COPYRIGHTED.** U.S. Government or Federal Rights License. All other rights and uses except those permitted by copyright law are reserved by the copyright owner.

☐ **DISTRIBUTION STATEMENT B.** Distribution authorized to U.S. Government agencies only. Other requests for this document shall be referred to controlling office.

☐ **DISTRIBUTION STATEMENT C.** Distribution authorized to U.S. Government Agencies and their contractors. Other requests for this document shall be referred to controlling office.

☐ **DISTRIBUTION STATEMENT D.** Distribution authorized to the Department of Defense and U.S. DoD contractors only. Other requests shall be referred to controlling office.

☐ **DISTRIBUTION STATEMENT E.** Distribution authorized to DoD Components only. Other requests shall be referred to controlling office.

☐ **DISTRIBUTION STATEMENT F.** Further dissemination only as directed by controlling office or higher DoD authority.

Distribution Statement F is also used when a document does not contain a distribution statement and no distribution statement can be determined.

☐ **DISTRIBUTION STATEMENT X.** Distribution authorized to U.S. Government Agencies and private individuals or enterprises eligible to obtain export-controlled technical data in accordance with DoDD 5230.25.

Final Technical Report

Grant: N00014-07-1-0503
Title: Oxide films for RF applications
Institution: Carnegie Mellon University
PI: M. Skowronski
Period: 01/06/07-03/31/08

The ONR award "Oxide films for RF applications" have been awarded and was worked on in collaboration with Electro Optics Center of Pennsylvania State University. All of the MBE growth experiments have been conducted at EOC facility in Freeport PA and in collaboration with EOC personnel: Drs. V. Heydemann and O. Maksimov among others. All publications resulting from this award were joint papers. The award had three tasks which are summarized in detail below.

Task 1. Identification of dielectric loss mechanisms in MBE oxide films

The proposed goal was to identify, isolate, and reduce sources of loss in thin film dielectrics. It is important to note that the loss in bulk single crystals is often orders of magnitude below that of their thin film counterparts. It is believed that defects in thin films that are not present in bulk single crystals are responsible for the greater loss in films. Likely candidates are increased point defect concentrations, dislocation arrays such as low angle grain boundaries, and the interaction between them. We have specifically investigated defects due to deviation from film stoichiometry (Sr/Ti ratio) in SrTiO_3 films. The incorporation of both excess A-site cations and excess B-site cations are of interest because locally non-stoichiometric regions may appear during any growth owing to local supply fluctuations. This could lead to locally defective structures which can perturb the physical properties. It was reported previously that excess Sr was incorporated into the growing $\text{Sr}_{1+\delta}\text{TiO}_{3+\delta}$ films via (001) planar defects that are similar to the (rock salt) SrO bi-layers that occur in the $\text{Sr}_{m+1}\text{Ti}_m\text{O}_{3m+2}$ Ruddlesden-Popper phases. Such Sr-excess films had much lower dielectric constants and tunabilities than stoichiometric SrTiO_3 films. Excess Ti in $\text{SrTi}_{1+\delta}\text{O}_{3+2\delta}$ films ($\delta > 0.04$) was observed to segregate to grain boundaries, as evinced by an increase in the measured Ti/O ratio at grain boundaries. Although slight Ti-excess ($\delta < 0.1$) did not affect dielectric properties significantly, both the dielectric constant and the tunability decreased with further deviation from the 1:1 ratio.

It should be noted that, in spite of the observations of grain boundary segregation in TiO_2 -excess SrTiO_3 films, there are potential mechanisms by which the perovskite structure can incorporate excess B-site cations into the bulk of the structure. BaTi_2O_5 is a ferroelectric phase that has been reported to have a structure related to the perovskite, wherein the excess TiO_2 is incorporated into the BaO planes of a perovskite (in a complicated ordered pattern). Nevertheless, there are no reports of an equivalent SrTi_2O_5 phase. In addition to this potential mechanism for TiO_2 incorporation into SrTiO_3 , one can envision a structure in which double TiO_2 layers, consisting of edge-sharing octahedra similar to those in anatase, alternate with SrO layers in a SrTi_2O_5 structure, if the film were deposited in a precise atomic layer

deposition mode and if the arrangement was either thermodynamically or kinetically stable. In this work, we use layer-by-layer molecular beam epitaxy (MBE) as a growth method to explore the stability of such global and local non-stoichiometries.

Films have been grown using atomic layer deposition (ALD), where the Sr(Ti) flux is alternated between being on(off) and off(on) and where full monolayers (MLs) of SrO and TiO₂ are sequentially deposited. The atomic fluxes were carefully calibrated prior to the growth to achieve high quality films. Knowing and maintaining a constant flux value throughout the growth is believed to be particularly important during ALD since the growth is not self-limited. Thus, deposition of any excess material over the monolayer coverage leads to local surface nonstoichiometries that, in the case of high Ehrlich-Schwoebel barriers and low interdiffusion between adjacent layers, can introduce defects into the growing film. In this work, we compare the MBE growth and the structure of films that are locally and globally stoichiometric with those that are globally non-stoichiometric.

The MBE grown films were deposited on LaAlO₃ (001) substrates (indexed using the pseudocubic perovskite notation). Prior to growth, substrates were etched in a 3:1 HCl:HNO₃ solution and then degreased ultrasonically in acetone and then ethanol for five minutes each. After loading into the MBE chamber, the substrates were annealed for one hour at 750° C under a purified ozone flux of 0.5 sccm (chamber pressure of 1.8×10^{-6} Torr). The same ozone flux and substrate temperature were also used for all film growth experiments described herein. A Ti flux was produced using two high-temperature Ti cells, each operating at 1550° C while the Sr flux was produced using a standard effusion cell operating at 470° C. The typical growth rate was approximately 10 nm/hour for a SrTiO₃ film. All films were grown to a nominal thickness of 200 monolayers (MLs), which for SrTiO₃ corresponds to ~ 39.1 nm. The growth mode was monitored *in-situ* by reflection high-energy electron diffraction (RHEED) using a Staib electron gun operating at 12 kV with an incident angle of ~3°. For locally and globally stoichiometric films, the Sr source was opened to deposit 1 ML of SrO for every monolayer of TiO₂. For globally non-stoichiometric films, the SrO deposition time was increased (decreased) for Sr-(Ti-) rich films and the Sr:Ti ratio was varied from 2:1 to 1:2.

Figures 1.1(a) and (b) show RHEED patterns taken along the [100] and [110] azimuths, respectively, for a stoichiometric SrTiO₃ film grown using the ALD method. A 1x1 unreconstructed surface is clearly evident. Sharp, narrow lines indicate the film has a flat surface with a large density of atomic steps, while the Kikuchi lines attest to the high crystal quality of the film. It should be noted that the RHEED intensity was monitored throughout the growth and regular RHEED oscillations were observed on the specular

reflection without any decay or modulation in intensity, supporting that the film is stoichiometric SrTiO_3 . Figure 1.1(c) and Figure 1.1(d) show RHEED patterns taken respectively for the $\text{SrTi}_{1+\delta}\text{O}_{3+2\delta}$ (slightly Ti-rich, $\delta \approx 0.05$) and $\text{Sr}_{1+\delta}\text{TiO}_{3+\delta}$ (slightly Sr-rich, $\delta \approx 0.06$) films, respectively. A 2x reconstruction (marked by arrows) is evident along the [100] azimuth in the case of Ti-rich film (Figure 1.1(c)); a similar 2x reconstruction is observed along the [110] azimuth (also marked by arrows) in the case of Sr-rich film (Figure 1.1(d)). These reconstructions clearly mark slight Ti or Sr excesses, and were previously used to adjust the composition during the MBE growth. It should also be noted that RHEED oscillations were observed at the initial stages of growth for both of these slightly off-stoichiometric films. In contrast to the stoichiometric film deposited using ALD to produce integer valued monolayers, the oscillation intensity gradually decreased throughout the growth of these latter non-stoichiometric films, owing to their fractional monolayer coverages.

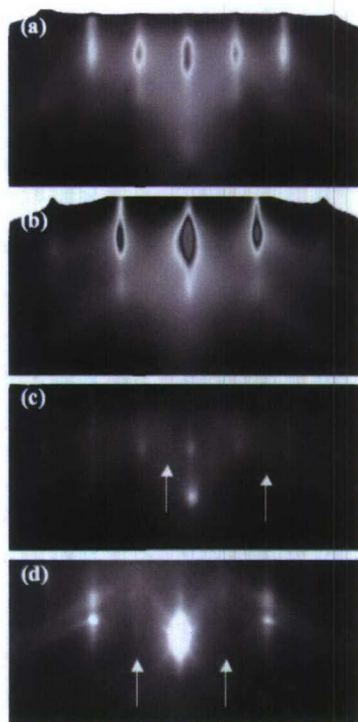


Fig. 1.1 RHEED patterns observed during growth of various films. (a) and (b) are from a stoichiometric SrTiO_3 film along the (a) [100] and (b) [110] azimuths. (c) is from the slightly Ti-rich SrTiO_3 film taken along the [100] azimuth. (d) is from the slightly Sr-rich SrTiO_3 taken along the [110] azimuth.

Figure 1.2 shows XRD θ - 2θ scans for the five films corresponding to (a) a stoichiometric SrTiO_3 film, (b) a slightly Ti-rich SrTiO_3 , (c) a 100% excess Ti-rich film, “ SrTi_2O_5 ”, (d) a slightly Sr-rich SrTiO_3 , and (e) a 100% excess Sr-rich film or “ Sr_2TiO_4 ”. In each pattern, the three dominant peaks located at 23.5° ,

48.0°, and 75.2° degrees correspond to (00 l) ($l = 1, 2, 3$) of the LaAlO₃ substrate (the peak marked with the * comes from the background). Figure 1.2(a) is from the stoichiometric film whose RHEED patterns were given in Fig. 1.1(a) and 1.1(b). In Fig. 1.2(a) only the (00 l) reflections of SrTiO₃ are observed. The out-of-plane lattice constant was calculated to be $c \sim 3.928$ Å, which is larger than the bulk lattice parameter (3.905 Å) of SrTiO₃, indicating that the film is only partially relaxed. While these 400 Å thick (nominally) films are well above the critical thickness (≈ 30 Å), partially relaxed films are frequently observed at this thickness. The intensity ratios of the (001)/(002) peaks and the (003)/(002) peaks are close to the expected values. These good-quality strained epitaxial films of stoichiometric SrTiO₃ are similar to others reported in the literature and serve as a baseline for comparison for the rest of the films grown in this work.

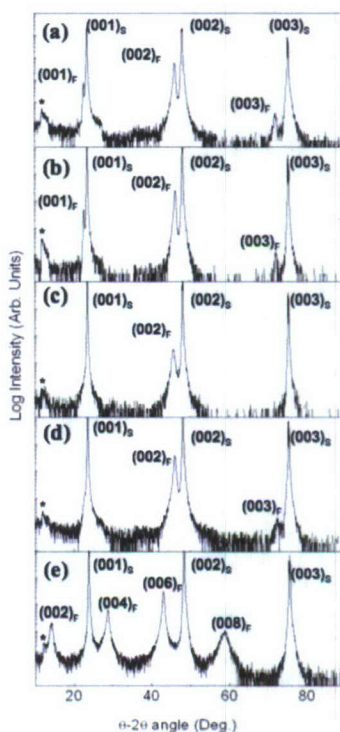


Fig. 1.2 XRD θ -2 θ scans obtained for (a) a stoichiometric SrTiO₃ film, (b) a slightly Ti-rich SrTiO₃, (c) a 100% excess Ti-rich film, “SrTi₂O₅”, (d) a slightly Sr-rich SrTiO₃, and (e) a 100% excess Sr-rich film or “Sr₂TiO₄.” All diffraction peaks are marked with (hkl) values, where the subscripts S and F denote respectively the substrate and film peaks. The peak marked with the * is due to the background.

Figure 1.2(b) and Figure 1.2(d) show θ -2 θ scans for, respectively, the slightly Ti-rich and slightly Sr-rich films whose RHEED patterns were shown in Fig. 1.1. While the XRD pattern of Ti-rich film is very similar to the XRD pattern of stoichiometric SrTiO₃, the XRD pattern of Sr-rich film shows weak intensities for the (001) and (003) peaks, as indicate by the (001)/(002) and (003)/(002) intensity ratios

shown in Table I. This decrease likely arises from the presence of additional rock salt SrO layers intergrown with the perovskite structure. Such stacking faults have been reported in Sr-rich films and lead to a diminished long-range order and diminished (001) and (003) peak intensities. Nevertheless, the out-of-plane lattice parameter determined in each case from these patterns is indistinguishable from the partially-strained stoichiometric SrTiO₃ film; each is in the range of 3.93 Å to 3.94 Å.

In Figures 1.2(c) and (e), θ -2 θ patterns taken from extremely Ti-rich (100% excess Ti) and extremely Sr-rich (100% excess Sr) films are respectively shown. While the slight excess Ti films showed no significant change in relative intensity of the (001), (002), and (003) peaks (with respect to the stoichiometric values), the extremely Ti-rich film shows greatly diminished (001) and (003) intensities and a slightly diminished (002) peak (see Table I). In addition, the out-of-plane lattice parameter of the film was 3.967 Å, significantly larger than any of the SrTiO₃ films discussed above. This pattern implies that a defective perovskite-like phase is present in this film with a stoichiometry that is different from SrTiO₃, and is discussed further below. The 100% excess Sr film has the appropriate stoichiometry for Sr₂TiO₄, a stable Ruddlesden-Popper phase; the XRD pattern shown in Fig. 1.2(e) corresponds well to that of an (001)-oriented epitaxial film of Sr₂TiO₄, and is indexed as such.

The rapid loss of long-range symmetry with a slight Sr-excess can be explained by the inclusion of Ruddlesden-Popper defects, that is, SrO double layers (i.e., as stacking faults) intergrown with the stoichiometric perovskite in the growing film. For the extremely Sr-rich films, these stacking faults order (there is one extra SrO layer for every perovskite SrTiO₃ layer) to produce the Sr₂TiO₄ phase as an epitaxial film. The structural response to a slight Ti excesses demonstrates no immediate loss of long-range symmetry and little evidence of Ti-incorporation into the bulk of the film, which can be explained by the slight Ti-excess moving to grain boundaries or amorphous regions, and/or to the upper surface, as evinced by the presence of the particular RHEED reconstruction shown in Fig. 1.1(d). However, for the extremely Ti-rich film, there is evidence that a loss of long-range symmetry occurred and that excess Ti was incorporated into a perovskite-like structure, which cannot be explained by any of these mechanisms. It is clear that some portion of the excess Ti has been incorporated structurally into the SrTiO₃ crystal, causing a decrease in the intensity of the (001) and (003) peaks as well as an increase in the overall lattice parameter. The XRD is not consistent with any novel-layered phase formation, but rather to a film on which the excess TiO₂ is incorporated somehow into the perovskite structure by mixing the SrO and TiO₂ layers. Such mixing is known to occur for a stoichiometrically related BaTi₂O₅ phase, but more work is necessary to understand the detailed structure of this film.

Task 2. Electron microscopy characterization of strain relaxation mechanisms in dielectric films.

The goal of Task 2 was to assess the effects of strain relaxation in dielectric oxide films on the crystalline quality of the film. Virtually all reports on $\text{Ba}_x\text{Sr}_{1-x}\text{TiO}_3$ films so far were focused on lattice mismatched epi/substrate systems and most films were either fully or partially relaxed with high extended defect densities. Random strains associated with dislocations are suspected to play a significant role in lower dielectric constants and tunabilities observed in films as compared to bulk crystals.

The materials of interest for RF applications: SrTiO_3 , BaTiO_3 , CaTiO_3 and their solid solutions all have perovskite structures. At temperatures in excess of 1000K, which is the typical film growth temperature, these materials crystallize in cubic phase. They are expected have similar deformation mechanisms and dislocations generated by deformation should have similar characteristics. In the past two decades, several groups addressed identification of the slip system in SrTiO_3 and BaTiO_3 single crystals and thin films. It is believed that the $\langle 100 \rangle$ slip direction is the most common with the $\langle 110 \rangle$ slip direction being the second but number of experimental observations are still not accounted for. Takeuchi *et al.* (1998) reported that in bulk plastically deformed SrTiO_3 prepared by crushing at room temperature all dislocations had $\langle 100 \rangle$ -type Burgers vectors. Yamanaka *et al.* (2000) showed that most of the dislocations in the as-grown single crystals have $\langle 100 \rangle$ type of Burgers vectors using both TEM and X-ray topography. However, Nishigaki *et al.* (1991), and Gumbsch (2001) *et al.*, they proved the dislocations in the deformed crystals have both $\langle 100 \rangle$ and $\langle 110 \rangle$ types of Burgers vectors. Matsunaga (2000) identified the slip system in SrTiO_3 to be $\langle 110 \rangle \{110\}$. For thin film strain relaxation mechanism, Suzuki (1999) reported that the misfit dislocations in the interface of BaTiO_3 and SrTiO_3 had the $\langle 110 \rangle$ -type Burgers vector and proposed that the misfit dislocations were generated by gliding through $\langle 110 \rangle \{110\}$ slip system. These results contradict with previous results from Chen *et al.* (1993), Stemmer *et al.* (1995), and Dai *et al.* (1996), who reported misfit dislocations with a $\langle 100 \rangle$ Burgers vector and the relaxation was proposed to occur through climb.

All of the above researches on films were based on the geometry of $[001]$ -oriented film grown on the cubic material (001) surfaces. In our experiments, we purposely chose an orientation in which $\langle 100 \rangle \{010\}$ slip system was favored i.e. growth on $[111]$ -oriented substrates. $\text{Ba}_{0.6}\text{Sr}_{0.4}\text{TiO}_3$ (BSTO) film composition was chosen because it is cubic above room temperature. Films have been deposited by pulsed laser deposition on $[111]$ -oriented SrTiO_3 substrates. Two dimensional layer-by-layer growth

mode were observed for the film growth using ex-situ AFM characterization methods and reflection high energy electron diffraction (RHEED). Film thicknesses were around 25 nm which is above the calculated critical thickness. Jeol 2000 conventional transmission electron microscopy (TEM) and Technai F20 high resolution TEM were used to analyze the dislocations in the film and at the film-substrate interface.

Fig. 2.1 (a) shows a plan view image of the $[111]$ -oriented film and part of the substrate. Three sets of straight dark contrast lines are visible corresponding to misfit dislocations network at the epi/substrate interface. Compared the dislocation line directions with the selected area diffraction pattern (SADP), the misfit dislocation lines lie along $\langle 11\bar{2} \rangle$ directions. This is inconsistent with the generation by $\langle 100 \rangle\{010\}$ slip system as the $\{100\}$ planes intersect with $\{111\}$ interface along $\langle 110 \rangle$ directions.

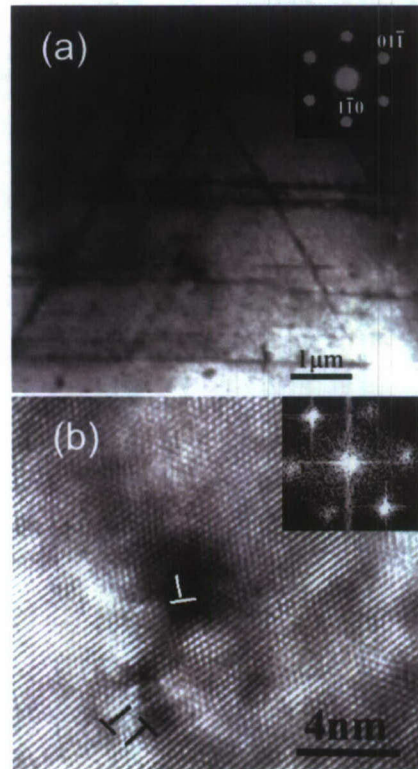


Fig. 2.1 (a) Conventional bright field image of $\text{BaxSr}_{1-x}\text{TiO}_3$ film grown on SrTiO_3 (111) substrate, the inset shows the corresponding selected area diffraction pattern. (b) High resolution plan view image of the threading dislocations in the BST film, the inset is the Fourier Fast transformation (FFT) of the image. The \top symbols mark the extra plane associated with the dislocations.

High resolution plan view TEM was used to image the threading dislocations in the volume of BST film at the very edge of the TEM sample where only the film was present. As shown in Fig. 1(b), the high resolution TEM images obtained along $[111]$ zone axis showed that the extra half planes associated with

the threading dislocations are $\{110\}$ planes. This indicates that the threading dislocations have Burgers vectors of $\langle 110 \rangle$ type. In Fig. 2.2, the point O represents the origin point of a unit cell. The OA, OB, and OC correspond to the $[100]$, $[010]$, $[001]$ directions. CD represents the dislocation line extending along $[11-2]$. $[001]$ (OC) has projection on (111) plane in $[11-2]$ direction which is parallel to dislocation line direction in which it cannot contribute to strain relaxation as a misfit dislocation. $[100]$ (OA) and $[010]$ (OB) directions cannot have projection of $\langle 1-10 \rangle$ component in (111) plane. $\langle 100 \rangle$ can only have projection of $\langle 11-2 \rangle$ -type, if that is the case the dislocations must be pure in-plane screw type. However, in-plane screw dislocations can not act as misfit dislocations and relax strain in the film. Only dislocations with edge component in the interface plane can act as misfit dislocations. Based on the above analysis, there is only one possibility which is that the misfit dislocations are edge dislocation with in-plane $\langle 1-10 \rangle$ Burgers vector components. As shown in Fig. 2.2, the dislocation line direction $[11-2]$ and the Burgers vector $\mathbf{a}[1-10]$ both lie in the (111) plane parallel to the interface. This configuration does not allow for dislocations to glide. The only possibility that the dislocation can move toward the interface is by climb which is kinetically limited by vacancy diffusion. There are three equivalent $\langle 11-2 \rangle$ directions, therefore, the dislocations form a triangular network. From Fig. 2.1, it is apparent that the average distance between misfit dislocations is about $0.5\sim 1\mu\text{m}$, which is much larger than the value (40nm) expected for a completely relaxed film. Here we find that even when the geometry favors the slip system $\langle 100 \rangle \{010\}$, this slip system was still not activated, instead the film chose a kinetically slow process to relax the strain. It seems to activate $\mathbf{a}\langle 100 \rangle$ types of Burgers vector to glide requires higher energy than to activate $\mathbf{a}\langle 1-10 \rangle$ climb.

For comparison, BST films on $[001]$ -oriented LaAlO_3 substrates were deposited using the same growth condition. Plan-view conventional TEM showed that the dislocation networks are exactly as those reported lying in the orientations of $\langle 100 \rangle$ (Fig. 2.3(a)). Cross-sectional HRTEM of the interface showed misfit dislocations with $\frac{1}{2}\mathbf{a}\langle 011 \rangle$ Burgers vectors. Stacking fault associated with two partials was observed, Burgers circuit around the two partials together gave an $\mathbf{a}\langle 010 \rangle$ Burgers vector. This observation is consistent with the relaxation model proposed by Suzuki (1999).

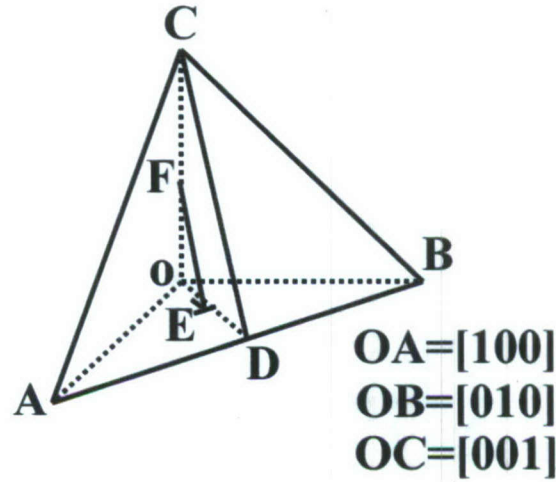


Fig. 2.2 Schematic of the geometry and relaxation mechanism in $[111]$ -oriented film. $OA=[100]$, $OB=[010]$, $OC=[001]$, $CD=[11-2]$, $OD=[110]$, $AB=[-110]$, EF represents one of the dislocation lines parallel to direction $[11-2]$, the Burgers vector is represented as \perp mark which is parallel to $[-110]$ direction.

In conclusion, in the case of $\langle 100 \rangle \{010\}$ -slip-system-favored $[111]$ -oriented film, $\langle 100 \rangle \{010\}$ slip system was not activated. Instead, climb of a $\langle 110 \rangle$ type dislocations was observed to act as strain relaxation mechanism. The results presented above, indicate that $\langle 110 \rangle \{1-10\}$ is the primary slip system in $(\text{Sr, Ba, Ca})\text{TiO}_3$ family of perovskite structures.

Task 3. New and Engineered Materials for Dielectric Constant Control

The proposed work called for deposition of nano-structured thin film superlattices of $(\text{AEO})_m(\text{TiO}_2)_n$ - type with varying m and n numbers in order to generate a homologous series of materials having artificially layered crystal structures. These homologues can display unique chemical bonding environments that could improve our understanding of tunability and loss in dielectrics. Specifically, it is hoped that the dielectric constant of two component $(\text{AEO})_m(\text{TiO}_2)_n$ superlattices is greatly enhanced compared to monolithic films and single crystals. It is also known that trilayer superlattices of these materials can be used to create self-poled, acentric, electro-optically active materials.

In this work, layer-by-layer (LBL) molecular beam epitaxy (MBE) has been used to produce superlattice films in the $(\text{SrO})_m(\text{TiO}_2)_n$ system ($m = 1-5$, $n = 1$). These crystals belong to a homologous series that can be written as $\text{Sr}_m\text{TiO}_{2+m}$ and that consist of m monolayers of SrO followed by a single monolayer of TiO_2 .

While the SrTiO_3 , Sr_2TiO_4 , and SrO ($m = 1, 2$, and ∞) members of this series are stable in the bulk form,^{7,8} the Sr_3TiO_5 , Sr_4TiO_6 , and Sr_5TiO_7 ($m = 3, 4, 5$) members have not been previously reported, nor have structures with the latter stacking arrangements been observed for many other oxides in bulk or film form. Triple and quadruple rock salt (A,A')O layers have, however, been observed in some systems, such as in cuprate superconductors containing $A = \text{Sr}, \text{Ba}$ and $A'\text{O} = \text{BiO}, \text{TlO}$, or HgO , and trilayers of CaO were observed in the misfit-layered oxide $\text{Ca}_3\text{Co}_4\text{O}_9$.

Figure 3.1 shows schematics of the unit-cells of the targeted artificially-layered phases ($m = 1 - 5$). The strontium (light spheres), titanium (centered in the octahedra), and oxygen (apices of the octahedra and dark spheres) ions are assumed to arrange in the same manner as in the related SrTiO_3 , Sr_2TiO_4 , and SrO ($m = 1, 2, \infty$) phases. Based on these principles, the c lattice-parameter of the unit cells for the odd m phases is equal to the spacing between TiO_2 planes (marked as d_T in Fig. 3.1), whereas c is twice d_T for the even m phases owing to a body-centering translation. Although these phases are easily envisioned, the question remains as to whether or not they can be formed and whether or not they are stable with respect to large scale phase separation into the equilibrium bulk phases Sr_2TiO_4 and SrO . The epitaxial films were grown on $\text{LaAlO}_3(001)$ substrates using our MBE system located at PennState Electro-Optics Center. The single crystal substrates were etched in a 3:1 $\text{HCl}:\text{HNO}_3$ solution for 2-3 minutes, rinsed with deionized water, and ultrasonically cleaned in acetone and ethanol for five minutes each. Substrates were annealed prior to the growth for one hour at 750°C under a purified ozone flow of 0.5 sccm (resulting in a chamber pressure of 1.8×10^{-6} Torr). The same conditions were also used for film growth. Growth was controlled to the monolayer level by first calibrating the flux rates of both sources *ex-situ*. Deposition was carried out by alternating the open elemental source between Sr and Ti (while the other was shuttered) in a manner to deposit m monolayers of SrO followed by a single TiO_2 monolayer, which was repeated for 50 growth cycles. Since some of the films have limited air stability ($m > 2$), films were capped with an epitaxial MgO overlayer that allowed for their facile X-ray characterization. Growth was monitored *in-situ* using reflective high energy electron diffraction (RHEED) and the films were characterized *ex-situ* using X-ray diffraction (XRD) and transmission electron microscopy (TEM).

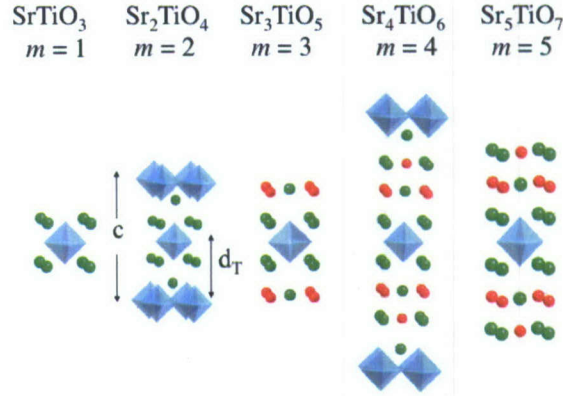


Fig. 3.1 Models of the known ($m = 1$, SrTiO_3 and $m = 2$, Sr_2TiO_4) and predicted ($m = 3$, Sr_3TiO_5 , $m = 4$, Sr_4TiO_6 , $m = 5$, Sr_5TiO_7) structures in the $\text{Sr}_m\text{TiO}_{2+m}$ series. The lighter spheres represent Sr^{2+} ions, the darker spheres represent O^{2-} ions which are not coordinated to a Ti^{4+} ion, and each octahedron represents a Ti^{4+} (at the center) coordinated to 6 O^{2-} ions (one at each corner).

In Fig. 3.2, θ -2 θ XRD spectra registered from the $m = 1, 2, 3, 4, 5$, and ∞ members of $\text{Sr}_m\text{TiO}_{2+m}$ series are shown. In each spectrum, the three most intense peaks arise from the (00 l) peaks of the $\text{LaAlO}_3(001)$ substrate (denoted with $L: l$), indexed using a pseudocubic notation. The (002) peak arising from the epitaxial MgO capping layer is marked as M in each pattern. The remaining peaks (except the background-related peak around 12° marked with a $*$) can all be indexed to a single family of diffracting planes, which are the (00 l) planes of the single-phase $\text{Sr}_m\text{TiO}_{2+m}$ films. These peaks are marked with their 00 l values and indicate the targeted phases can indeed be realized, as described below.

One should note the following trends in the XRD patterns. First, the peak representing the average spacing between adjacent atomic planes, which we call the fundamental reflection, is marked as (00 l) F (for SrTiO_3 this is marked as (002) F). The location of this fundamental peak moves to a lower 2θ angle with increasing m (from 46.52° for $m = 1$ to 38.44° for $m = 5$). This is an expected result because the average interplanar spacing (d_F) has an increasing contribution from adjacent SrO-SrO layers as m increases. The known SrO-SrO interplanar distances range from 2.39 Å in Sr_2TiO_4 to 2.58 Å in SrO, both of which are much larger than the known SrO-TiO $_2$ interplanar distances of ≈ 1.95 Å found in SrTiO_3 and Sr_2TiO_4 . With an increasing number of SrO layers, a larger portion of the adjacent interplanar spacings come from the wider SrO-SrO spacings, and therefore the average interplanar spacing increases as well. The values of d_F determined from these patterns are 1.95, 2.09, 2.29, 2.32, 2.34, and 2.57 Å for the $m = 1, 2, 3, 4, 5$, and ∞ films, respectively. Based on these values, we can determine the thickness associated with the SrO layer added to the $m-1$ phase; these are (in Å) N/A, 2.37, 2.89, 2.44, 2.42, and N/A for the $m = 1, 2, 3, 4, 5$, and ∞ films. Note that there is a large jump of 2.89 Å for the addition of an SrO layer from

the $m = 2$ phase to the $m = 3$ phase, a value that is actually larger than the bulk SrO lattice parameter. This indicates that relaxations also occur in the pre-existing SrO monolayers, allowing the effective increase to be greater than known SrO layer spacings. More detailed investigations are required to determining the precise interplanar distances.

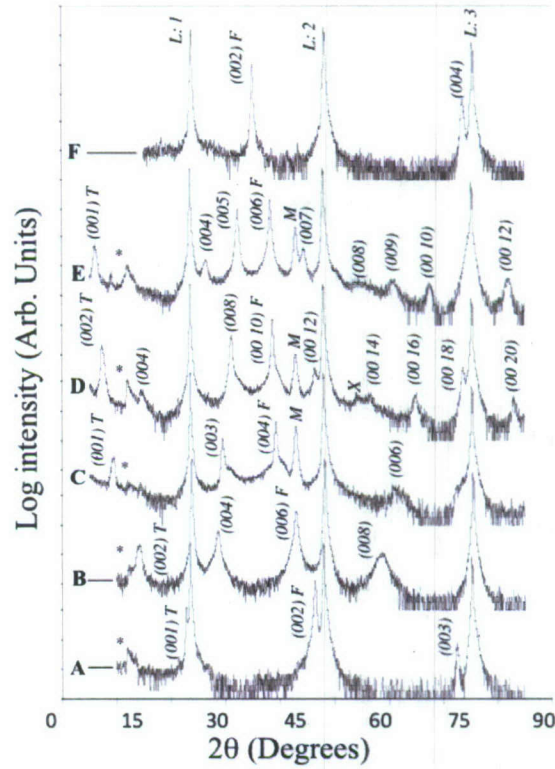


Fig. 3.2 X-ray diffraction patterns registered on film grown on $\text{LaAlO}_3(100)$ substrates from (A) SrTiO_3 , (B) Sr_2TiO_4 , (C) Sr_3TiO_5 , (D) Sr_4TiO_6 , (E) Sr_5TiO_7 , and (F) SrO

Second, the first peak in every pattern is a strong peak that represents the average distance between TiO_2 layers (or d_T) in these artificial crystals; these are marked as $(00l)T$ (for SrTiO_3 this is the (001) and is marked as $(001)T$). As expected, this peak shifts to dramatically smaller angles with increasing m (from 22.88° for $m = 1$ to 6.24° for $m = 5$) as the TiO_2 planes become further separated. From a unit-cell perspective, this interplanar spacing is equal to the c -lattice parameter ($\frac{1}{2}c$) for the even m (odd m) compositions. The values of d_T (and the increase from the prior value) determined from these patterns are 3.89 (N/A), 6.27 (2.38), 9.17 (2.9), 11.81 (2.64), and 14.16 (2.35) Å (Å) for the $m = 1, 2, 3, 4$, and 5 films, respectively. As the d_T values get larger, the error on those values increases. Nevertheless, the changes in these values also indicate again that a substantial relaxation in the SrO distances occurs on going from the $m = 2$ to $m = 3$ phase.

The observed value of m for the $(\text{SrO})_m(\text{TiO}_2)$ films can be compared to the nominal value targeted during deposition using the following expression:

$$m = d_T/d_F - 1$$

where d_T/d_F represents the observed average number of monolayers per period and the one represents the TiO_2 monolayer in the period. The observed values of m were 0.99(1), 1.99(3), 3.01(4), 4.09(8), and 5.05(9) for the $m = 1, 2, 3, 4$, and 5 films, respectively (with the parenthetical values representing the error in the last digit). It should be noted that the values of d_T , and therefore of m , become more sensitive to errors in measurement as the peak moves to lower angles. Nevertheless, the observed m values are well within the measurement error and are in good agreement with the targeted values. Note that there is nothing peculiar about the transition from the $m = 2$ to $m = 3$ phase, indicating that the large relaxations are not associated with an error in growth periodicity or composition. These results indicate that we have achieved the desired artificially layered crystal structures based on the monolayer arrangements induced by alternating MBE growth and that the films have excellent average long-range order.

From the $(00l)$ peaks, the c lattice parameters for the new phases Sr_3TiO_5 , Sr_4TiO_6 , and Sr_5TiO_7 , were determined to be 9.14, 23.55 Å ($1/2 c = 11.78$), and 14.60 Å, respectively. Asymmetric XRD scans were performed on the samples to measure the in-plane lattice parameters. All measurements were made on $\{10l\}$ peaks with $l = 1-4$; however, for crystallographic reasons, phases with even values of m have no intensity for $\{10l\}$ planes with even values of l . Figure 3.3 shows a lattice parameters (determined from the X-ray scans described above) as a function of m . In the figure, the open circles at $m = 1$ and $m = 2$ are literature data points for bulk phases, while the closed circles represent data points measured from the films with θ - 2θ scans shown above. Note that the a values measured for the SrTiO_3 ($m = 1$) and Sr_2TiO_4 ($m = 2$) films are lower than the bulk values; an in-plane contraction is expected given the smaller (3.79 Å) lattice parameter of the $\text{LaAlO}_3(001)$ substrate. As observed in the c -axis parameter, the largest change occurs on going from the $m = 2$ to $m = 3$ phase. For each of the Sr_3TiO_5 , Sr_4TiO_6 , and Sr_5TiO_7 phases, the a lattice parameter is found to not only be much lower than the values for SrTiO_3 and Sr_2TiO_4 (both close to 3.9 Å), but also lower than the substrate lattice parameter (3.79 Å for LaAlO_3). This implies that any epitaxial strain would leave these films in tension (with relaxed a lattice parameters of these films being lower than the measured values). Furthermore, the large change from $m = 2$ to $m = 3$ in both lattice parameters may be associated to this transition in the strain state on the films, although further structural characterization is required. Finally, at the lower right of the figure, the relaxed bulk lattice parameter of SrO is marked (using the primitive tetragonal cell). This set of data indicates with increasing number of

SrO monolayers per growth cycle, there is an in-plane relaxation toward the bulk lattice parameter of SrO, as expected.

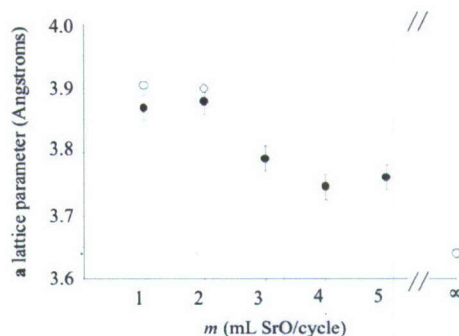


Fig. 3.3 In-plane (a) lattice parameters of the phases of the $\text{Sr}_m\text{TiO}_{2+m}$ series plotted as a function of m

Figure 4(a) shows a Fourier-filtered cross-sectional HRTEM image of the Sr_5TiO_7 film taken from the [100] zone axis in which the expected layer sequence can be observed, and Fig. 4(b) shows an enlarged view of the outlined region in (a). The vertical line in Fig. 4 (b) follows the [001] direction of the film, with the hashes marking the regions between bright columns for each (001) monolayer (detailed simulations will be presented elsewhere). The periodicity in the structure is captured best by the darkest, horizontal features (marked by arrows in Fig. 4(a)) that are parallel to the (001) plane. These features repeat every sixth layer in the micrograph, or about every 14 Å, in similar fashion to the expected periodicity of the TiO_2 monolayer that was measured to be 14.16 Å by XRD. In addition, the image has the expected lateral translational symmetry between layers for a phase with an odd value of m , or in other words there is no doubling of the unit cell owing to a body centering translation.

The results presented above clearly illustrate that artificially layered crystals in the homologous series $\text{Sr}_m\text{TiO}_{2+m}$ can be realized and they conform to the expected rock-salt/perovskite intergrowth structures. Such multiple (> 2 consecutive) rock-salt layers are not observed in any known phases in the SrO- TiO_2 system, even as extended defects. The question arises as to the nature of their stability. It is important to recognize that Sr_2TiO_4 and SrO are the stable phases for the compositions with $3 \leq m < \infty$. In order for these epitaxially layered films to phase separate, either the layers can coarsen, requiring massive diffusion, or they can recrystallize entirely, requiring both diffusion and nucleation. The latter is unlikely owing to the considerable barriers involved.

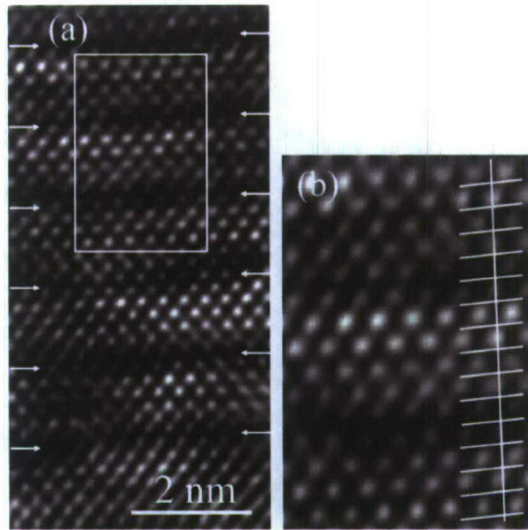


Fig. 3.4 (a) Fourier-filtered cross-sectional TEM image from the Sr_5TiO_7 film taken along the $[100]$ zone axis and (b) magnified view of the outlined region

In order to determine general properties and stability of oxide superlattices, a series of $(\text{SrO})_m(\text{TiO}_2)_m$ films with a range of m values ($2 \leq m \leq 33$) was grown by MBE. Two approaches were used: a typical Atomic Layer Deposition (ALD) approach and a modified ALD approach (MALD). In standard MBE growth (reactive co-evaporation), the Sr and Ti fluxes are equal and always on. In ALD growth, the Sr and Ti fluxes are alternated between being on and off with the dose per cycle corresponding to full monolayers (MLs) of SrO and TiO_2 as shown schematically in Figure 3.5(a). The ALD technique is of particular interest because it allows for the fabrication of novel phases and artificial superlattices, as well as allowing one to control the local stoichiometry precisely. Regardless of the approach, the atomic fluxes must be carefully calibrated prior to the growth to achieve high quality films. Knowing and maintaining a constant flux value throughout the growth is believed to be particularly important during ALD since the growth is not self-limited. Thus, deposition of any excess material over the monolayer coverage leads to local surface nonstoichiometries that, in the case of high Ehrlich-Schwoebel barriers and low interdiffusion between adjacent layers, can introduce defects into the growing film.

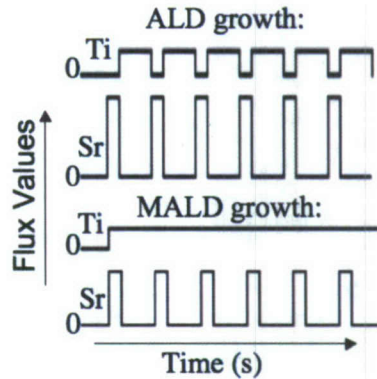


Fig. 3.5 Schematic representation of the different growth techniques used for the MBE growth. (a) represents atomic layer deposition (ALD) in which the Sr and Ti fluxes are alternated between being on and off. (b) represents the modified-ALD in which the Ti flux is kept constant and Sr is switched on and off. All growth is performed with the same ozone flux.

In the modified approach, which is illustrated in Figure 3.5(b), one source (Ti) is left open throughout the entire film growth process and the other source (Sr) is shuttered at a regular interval to provide specific monolayer coverages and to attain specific overall stoichiometries. Note that to maintain the overall film stoichiometry, the flux from the open source must be significantly lower than that from the shuttered source. The MALD technique allowed us to eliminate substrate temperature fluctuations that were unavoidable when shuttering the high-temperature Ti effusion cells. In this work, the Ti flux was close to $\frac{1}{4}$ the Sr flux.

All films grown in this work can be described by the formula $(\text{SrO})_m(\text{TiO}_2)_n$, the meaning of which is illustrated by Figure 3.6. The x-axis represents the number (m) of SrO monolayers (ML) deposited per cycle and the y-axis represents the number (n) of TiO_2 monolayers deposited per cycle. As examples, the phases SrTiO_3 and Sr_2TiO_4 are represented respectively by the $m,n = 1,1$ and $2,1$ points in the figure. Triangles are located in the figure at points where films were grown, using both ALD and MALD approaches, and the large arrow points along the line of stoichiometric films described below (where $m (=n)$ ranges from 2 to 33).

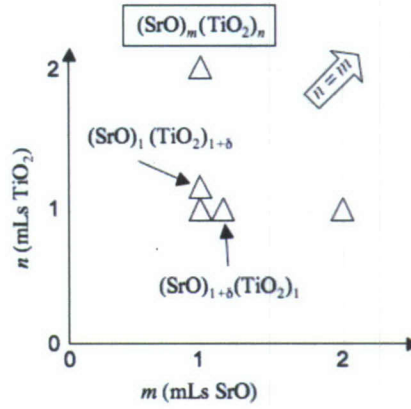


Fig. 3.6 Schematic compositional map for MBE grown $(\text{SrO})_m(\text{TiO}_2)_n$ films, where m (n) represents the number of monolayers of SrO (TiO_2) deposited per cycle (of either the ALD or MALD technique). The triangles represent films grown in this work for the $m, n < 2, 2$ region; the large arrow indicates that films were grown along the $m = n$ line for much larger values ($m = n \leq 33$).

For locally and globally stoichiometric films, the Sr source was opened to deposit 1 ML of SrO for every monolayer of TiO_2 (whether in the ALD or MALD method). For globally non-stoichiometric films, the SrO deposition time was increased (decreased) for Sr-(Ti)-rich films and the Sr:Ti ratio was varied from 2:1 to 1:2. To achieve films with a local non-stoichiometry and a global 1:1 stoichiometry, several (m) MLs of SrO were deposited followed by the same number (m) of TiO_2 MLs, and the sequence was then repeated until the total film thickness was reached. In the case of ALD, the growth sequence corresponded to the deposition of a $[(\text{SrO})_m/(\text{TiO}_2)_m]_{100/m}$ superlattice, where m was varied from 1 to 33.

Fig. 3.7 shows the RHEED line scan taken along the $[100]$ azimuth for the initial cycle of the MALD film with 10 monolayers of SrO and 10 monolayers of TiO_2 deposited per cycle (which is representative of all the films grown in this series). To register a RHEED line scan, a line is placed horizontally across a RHEED image and intensity at each point along the line is recorded with respect to time. At the initiation of the MALD grown films ($t = 0$ s), both the Sr and Ti shutters are opened; the initial jump in intensity everywhere along the line at $t = 0$ is due to the opening of the high-temperature Ti cells. The substrate RHEED pattern quickly disappears, after only 2-3 total monolayers (remembering that the film at this point is largely SrO rich). This indicates that the long-range surface structure periodicity was lost soon after growth initiation. At $t = 400$ s the Sr shutter was closed and the film stoichiometry gradually moved toward the Sr:Ti = 1:1 value. The diffuse RHEED streaks re-appeared in the line scan; moreover, the position of the RHEED intensity corresponded to that expected from a crystalline, epitaxial SrTiO_3 surface. The time period shown in Fig. 3.7 corresponded to deposition of 10 MLs of SrO and the same

number of monolayers of TiO_2 . This growth cycle was repeated 10 times for this film to achieve the total film thickness of 100 monolayers of each SrO and TiO_2 .

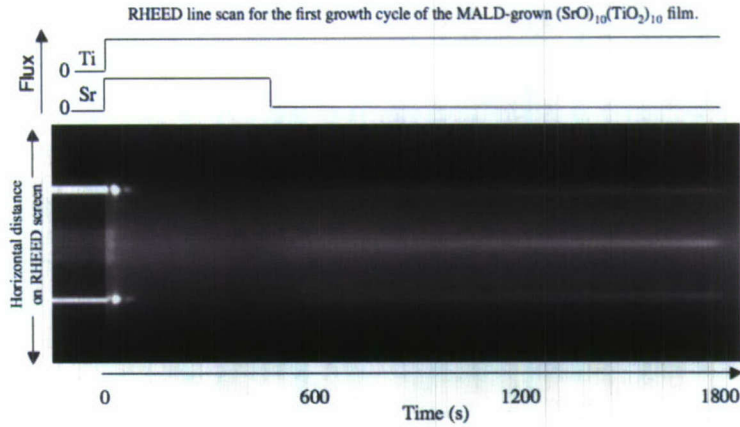


Fig. 3.7 RHEED line scan taken along the $[100]$ azimuth for the first growth cycle of the MALD-grown $(\text{SrO})_{10}(\text{TiO}_2)_{10}$ film. The intensity initially decreases but returns by the end of the cycle.

From the figure, it is clear that the surface of the growing film exhibits a RHEED pattern that is consistent with that of crystalline, epitaxial SrTiO_3 , when the film approaches a 1:1 Sr:Ti stoichiometry. For this to occur, there must be significant interdiffusion of the cationic components; Sr^{+2} ions must diffuse to the surface (or Ti^{+4} ions must diffuse into the SrO) in large numbers despite the fact that close to six-monolayers of Ti were deposited after the Sr shutter was closed. After each cycle, the RHEED patterns registered along the $[100]$ and $[110]$ azimuths were consistent with a flat, crystalline SrTiO_3 films. Along the $[100]$ azimuth, there was a visible two-fold reconstruction, which is indicative of a Ti-rich film. Since the outermost layers are Ti-rich using the MALD technique, this is not surprising. Either there is a persistent local Ti-rich non-stoichiometry owing to incomplete homogenization of the global cationic stoichiometry or there is a slight global excess of Ti-in these nominally stoichiometric films.

Ex-situ XRD θ -2 θ scans shown in Fig. 3.8 confirm the formation of perovskite SrTiO_3 for the locally nonstoichiometric $[(\text{SrO})_m(\text{TiO}_2)_m]_{100/m}$ films with $m = 8, 10, 20$, and 33. Figure 3.8(a) shows the XRD pattern for the ALD grown film (i.e., $m = 1$) for comparison. Scans from $m = 8, 10$, and 20 films are very similar to that of the stoichiometric SrTiO_3 ($m = 1$) film, confirming the presence of (001)-oriented SrTiO_3 as the only phase observable with XRD. While the $[(\text{SrO})_{33}(\text{TiO}_2)_{33}]_3$ film also exhibits a majority of (001)-oriented SrTiO_3 , an additional peak is observed at 32.4° . It can be assigned to (110)-oriented SrTiO_3 , indicating that for the largest m value some misoriented perovskite grains appear. What is striking in all these patterns is that there are no peaks arising from either SrO (expected at 34.8°) or any of the

forms of TiO_2 (a peak at 37.9° from (001)-oriented anatase is most likely). Their absence implies that the SrO- and TiO_2 -layers reacted in the solid state to form single-crystalline, epitaxial SrTiO_3 .

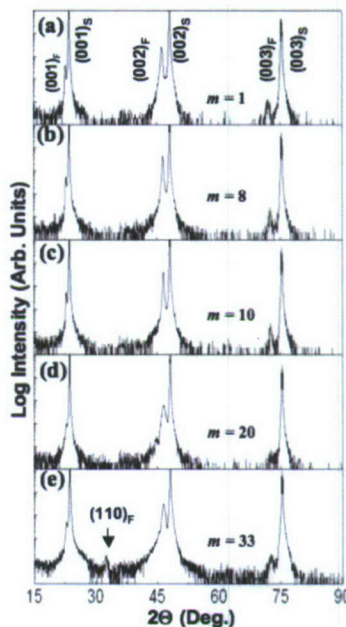


Fig. 3.8 XRD θ - 2θ scans registered for the $[(\text{SrO})_m(\text{TiO}_2)_m]_{100/m}$ series of films: (a) ALD SrTiO_3 ($m = 1$), (b) $[(\text{SrO})_8(\text{TiO}_2)_8]_{12}$ ($m = 8$), (c) $[(\text{SrO})_{10}(\text{TiO}_2)_{10}]_{10}$ ($m = 10$), (d) $[(\text{SrO})_{20}(\text{TiO}_2)_{20}]_5$ ($m = 20$), and (e) $[(\text{SrO})_{33}(\text{TiO}_2)_{33}]_3$ ($m = 33$). Peaks are marked in (a) for all patterns.

The (001)/(002) and (003)/(002) intensity ratios of these locally non-stoichiometric films, all given in Table I, were close to that observed for the SrTiO_3 ($m = 1$). It was shown earlier that slightly Sr-rich films and extremely Ti-rich films tend to have much diminished ratios. This argues further for the growth of good quality SrTiO_3 . Two important changes were observed to be correlated with increasing layer thickness. Firstly, the location of the film's (002) perovskite peak shifts to a slightly higher angle with increasing layer thickness. Secondly, the peaks become noticeably broader for larger values of m . These latter two observations are quantified in Figures 3.9 and 3.10.

Table I. Ideal and experimental relative intensity (I_{hkl}^R) values of (00 l) SrTiO₃ peaks. The relative intensities are normalized to the actual intensity (I) for the (002) peak (e.g., $I_{002}^R = I_{002} / I_{002} = 1$). All values are given for the ALD films.

Film	I_{001}^R	I_{003}^R	Film	I_{001}^R	I_{003}^R
SrTiO ₃ ^{ideal}	0.093	0.0089	SrTiO ₃	0.096	0.0069
Sr _{1+δ} TiO _{3+δ}	<0.02	<0.002	[(SrO) ₈ (TiO ₂) ₈] ₁₂	0.097	0.0050
SrTi _{1+δ} O _{3+2δ}	0.126	0.0056	[(SrO) ₁₀ (TiO ₂) ₁₀] ₁₀	0.112	0.0051
SrTi ₂ O ₅	<0.02	<0.002	[(SrO) ₂₀ (TiO ₂) ₂₀] ₅	0.110	0.015
Sr ₂ TiO ₄ [*]	0.11 [*]	0.31 [*]	[(SrO) ₃₃ (TiO ₂) ₃₃] ₃	0.096	0.0024

*Note that the Sr₂TiO₄ intensities correspond to the I_{002}^R and I_{004}^R , respectively, normalized to the I_{006} of the Ruddlesden-Popper structure. The ideal values for these are: 0.10 and 0.50, respectively, which compare well to the measured values.

In Fig. 3.9, the lattice parameters (determined from the 2θ location of all the films' (002) peaks) are plotted as a function of m values for films grown by both the ALD (filled circles) and MALD (open circles) methods. The bulk lattice parameter of SrTiO₃ is 3.905 Å, as indicated by the horizontal dashed line. For the films with m between ½ and 6 MLs, the c lattice parameters ranged between 3.93 Å and 3.94 Å, indicating that all of these films were only partially relaxed. Partial relaxation was confirmed by the fact that the in-plane lattice parameter (not shown) was smaller than the out-of-plane lattice parameter. However, for all films grown with layer thicknesses of at least 8 monolayers, the films were completely relaxed with their out-of-plane lattice constant scattered around the expected value of the bulk (the in-plane lattice parameter measurements confirmed that they were relaxed). It is also notable that the peak locations for films grown by the ALD method are in good agreement with the peak locations for the films grown by the MALD method. In other words, the film lattice parameters were similar regardless of which growth method was used.

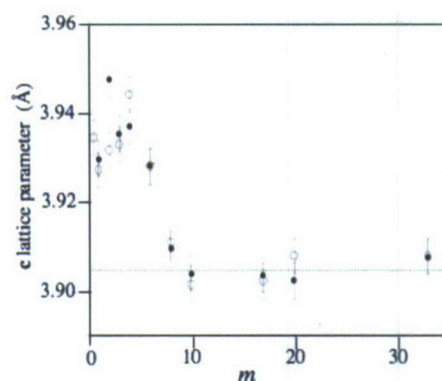


Fig. 3.9 Out-of-plane lattice constant, c , of $[(\text{SrO})_m(\text{TiO}_2)_m]_{100/m}$ films plotted as a function of m . The bulk lattice constant of SrTiO_3 is represented by the dashed horizontal line at $c = 3.905 \text{ \AA}$. Filled (open) circles represent ALD (MALD) films.

The (002) 2θ peak FWHMs are shown with respect to m in Fig. 3.10 for the structures grown by both ALD and MALD. Although there is a significant amount of scatter in the data, 7 of the 9 films having low m values of $\frac{1}{2}$ to 6 MLs had FWHMs in the range of 0.37° to 0.50° (with the two outliers being even wider). The four films grown with layer thicknesses of 8 and 10 monolayers had relatively narrow peaks, ranging from 0.25° to 0.35° . Three of these four films showed the three narrowest peak widths, and all four films were among the narrowest five measured peak widths. The films grown with $m = 17$ to 33 MLs had wider peaks, ranging from 0.35° to 0.72° . It is notable that the films grown with 8 monolayer thick layers were the first fully relaxed films and also exhibited some of the narrowest FWHM values. One explanation for this behavior is films having very thin layer thicknesses exhibit broader FWHMs owing to the fact that they are only partially relaxed and have distribution of misfit dislocations in the films that have not reached the film/substrate interface. On the other hand, the fully relaxed films with intermediate layer thicknesses have a larger fraction of misfit dislocations restricted to the interface and therefore exhibit narrower diffraction peaks. For the fully relaxed films with $m > 10$, the broader diffraction peaks probably arise from regions of decreased crystalline quality owing to the long diffusion distances necessary for complete reaction to take place.

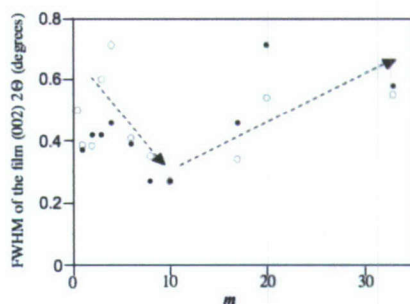


Fig. 3.10 Full width at half maximum of rocking curve of (002) peak of $[(\text{SrO})_m(\text{TiO}_2)_m]_{100/m}$ films plotted as a function of m . Open (filled) circles represent ALD (MALD) films.

While no XRD peaks were observed from SrO or TiO_2 phases, disordered or amorphous regions of SrO or TiO_2 (or regions of very SrO- or TiO_2 -rich material) may be present in films. Furthermore, some remnants of the initial ALD/MALD sequence may be present, particularly if the SrO and TiO_2 layers did not fully react. X-ray reflectivity measurements were carried out to explore if any periodic remnants were observable in the electron density. Figure 3.11 shows X-ray reflectivity scans for films grown with varying m . In Fig. 3.11(a), distinct oscillations and a relatively slow overall decline in intensity are observed for the ALD SrTiO_3 film ($m = 1$), indicating that this film has an atomically sharp film/substrate interface and a flat film/vapor surface. The oscillatory pattern was modeled using X'Pert Reflectivity software (version 1.2, PANalytical B.V., Netherlands). The pattern was fit well with a film thickness of 410 Å (and film surfaces that were 1 Å rough), which is close to (+4%) the 394 Å expected thickness of a 100 unit cell thick SrTiO_3 film with this strain state.

The reflectivity scans of films grown with $m > 1$ are given in Figs. 3.11(b) – 3.11(d). Each scan shows one set of oscillations that are very similar to those observed in Figure 3.11(a), corresponding to the overall thickness of the film and indicating that each of these block-grown films have a similar thickness and a similar surface roughness to the basic SrTiO_3 film. The refined thicknesses of these films are (a) 410 Å, (b) 455 Å, (c) 435 Å, and (d) 460 Å. In addition to the oscillations arising from the overall thickness of the films, another set of oscillations is evident in each pattern; these oscillations are marked by * in each scan. Their periodicity is correlated directly to the growth cycle periodicity. For example, in Fig. 3.11(d) the intensity of every fifth oscillation is visibly increased; these oscillations correspond to the five cycles carried out in growth (every cycle containing 20 monolayers each of SrO and TiO_2). Therefore, it is clear that there is some remnant crystallographic region that exists in the films that has a period equal to the growth period ($100 / m$) for the fully relaxed films.

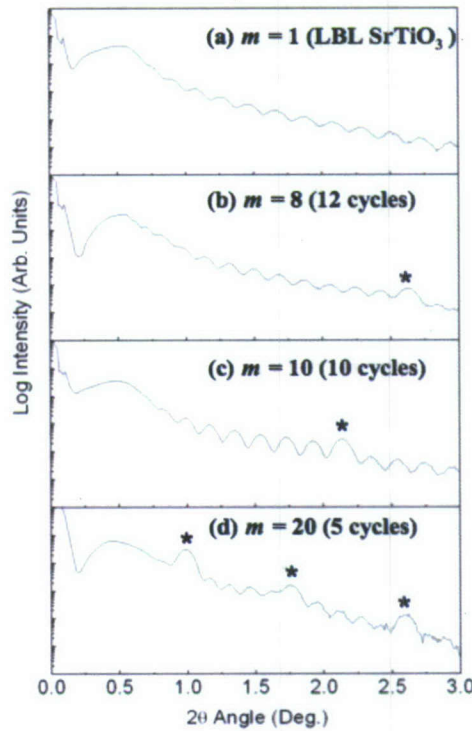


Fig. 3.11 X-ray reflectivity patterns registered from stoichiometric (a) SrTiO_3 ($m = 1$), (b) $[(\text{SrO})_8(\text{TiO}_2)_8]_{12}$ ($m = 8$), (c) $[(\text{SrO})_{10}(\text{TiO}_2)_{10}]_{10}$ ($m = 10$), and (d) $[(\text{SrO})_{20}(\text{TiO}_2)_{20}]_5$ ($m = 20$) films.

To observe the source of this periodic crystallographic perturbation, transmission electron microscopy (TEM) was used on both $m = 1$ and $m = 10$ films. Figure 3.12 shows both (a) a high-resolution image containing the film and substrate (taken along the $[100]$ zone axis) and (b) a selected area diffraction (SAD) pattern taken from the same region of this cross-section of the MALD SrTiO_3 ($m = 1$) film. In Figure 3.12(a), an atomically flat interface is clearly visible between the film and substrate, and no obvious defects are observed in the film. In the SAD image of Fig. 3.12(b), diffraction spots from both substrate and film are visible. The structures are very similar and the film is epitaxial, so the diffraction spots are very close together. However, the slightly larger lattice parameter of the SrTiO_3 film results in the associated diffraction spots being slightly inside the substrate spots. Note that the film spots are slightly more split from the substrate spots in the vertical direction since this corresponds to the out-of-plane strained direction. In addition, the film diffraction spots are larger, indicating that the crystalline quality of the film is lower than that of the single crystal substrate. Overall, these images further support the high-quality of the $m = 1$ films.

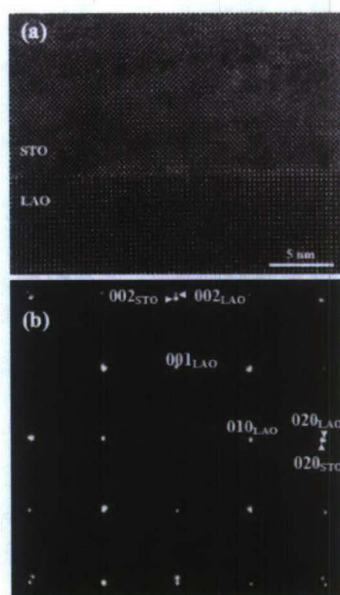


Fig. 3.12 TEM results from a cross-sectional MALD SrTiO₃ ($m = 1$) film deposited on a LaAlO₃(001) substrate. (a) is a lower resolution image taken from the film/substrate interface along the [100] zone axis. (b) is the selective area diffraction pattern taken from the region shown in (a). The pattern given in (b) is indexed using a cubic perovskite cell for both the film and substrate.

Figure 3.13 shows both (a) a TEM image containing the film and substrate (taken along the [100] zone axis) and (b) a SAD pattern taken from the same region of this cross-section of the MALD [(SrO)₁₀(TiO₂)₁₀]₁₀ ($m = 10$) film. In the low-resolution TEM image given in Fig. 3.13(a), arrows indicate the presence of visible boundaries that occur periodically throughout the film at the same frequency as the MALD cycling. The basic SAD pattern taken from this region is similar to that shown for the SrTiO₃ film in Fig. 3.12(b); however, faint additional spots are observed along the out-of-plane axis in Fig. 3.13(b) for the $m = 10$ film, which correspond to a longer-range periodicity. These spots are better seen in Figure 3.13(c) and the spot separation corresponds to a real-space length of about 40 Å or about a block of 10 monolayers of SrTiO₃. In other words, these diffraction spots correspond to the growth cycle periodicity.

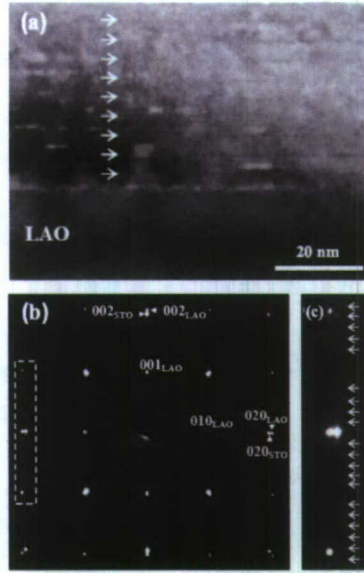


Fig. 3.13 TEM results from a cross-sectional MALD $[(\text{SrO})_{10}(\text{TiO}_2)_{10}]_{10}$ ($m=10$) sample on a $\text{LaAlO}_3(001)$ substrate. (a) is the high resolution image taken from the film/substrate interface along the $[100]$ zone axis. (b) is the SAD pattern taken from the region shown in (a) and (c) is a magnification of the outlined region in (b) showing the observed additional diffraction spots. The SAD pattern is indexed as in Fig. 3.12.

In Fig. 3.14, a high resolution TEM image taken for a region similar to the one shown in Fig. 3.13(a) is given for the same film. Once again, arrows are used to mark the location of each tenth of the film, corresponding to the approximate growth cycle periodicity. The dark horizontal features that appear at regular intervals (closely matched with the arrows) are clearly related to the growth method, and are likely stacking faults associated with a local excess of either Ti or Sr relative to the perovskite 1:1 cation stoichiometry. The regular and atomically flat nature of these features points to the following growth model: epitaxial SrTiO_3 nucleation at the SrO/TiO_2 interfaces which grows with a flat reaction front until the available reactants are consumed. The vast majority of the film consists of a highly crystalline SrTiO_3 matrix, which is continuous through the film in the out-of-plane direction, and the minority of the film corresponds to stacking faults that occur at the location of the growth cycle termination. It is important to realize that these imperfections correspond to individual monolayers that have slightly different electron densities than the matrix phase and not to completely unreacted regions of SrO and TiO_2 .

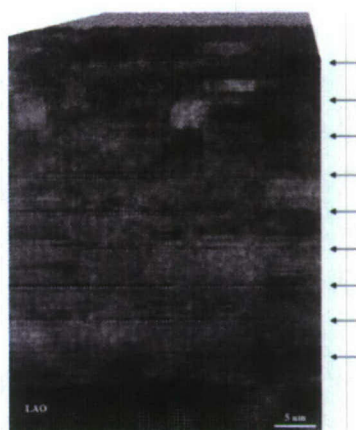


Fig. 3.14 HR-TEM image taken from a cross-sectional MALD $[(\text{SrO})_{10}(\text{TiO}_2)_{10}]_{10}$ ($m = 10$) sample on a $\text{LaAlO}_3(001)$ substrate along the $[100]$ azimuth of the film and substrate. The arrows are spaced at a distance equal to $1/10$ of the film thickness, equal to the growth periodicity, and align well with the location of observed stacking faults.

There are several worthwhile points to be made here. The first is that, although ALD-MBE has been used successfully to grow a large number of artificial structures and superlattices, no such layered structures could be obtained by alternating the growth of identical numbers of SrO and TiO_2 monolayers, even up to 33 MLs for each. In all cases studied here, the two layers inter-reacted to form SrTiO_3 perovskite films (with at most a residual atomic-layer stacking fault left at the original superperiod boundaries). At least one (and maybe both) of two things must be true for this to occur: the driving force must be high or/and the diffusion barriers must be low compared to the known cases of successful artificial layering.

That the driving force is high is not surprising, since SrTiO_3 has a large negative free-energy of formation from the oxides SrO and TiO_2 ; this can be approximated by the enthalpy of formation, which is ≈ -59.5 kJ/mol in the standard state. Conventional superlattices, such as $\text{SrTiO}_3/\text{BaTiO}_3$ superlattices, are built from similar compounds and their driving force for inter-reaction is the smaller free energy of mixing; this can be approximated by the configurational entropy for mixing equal numbers of two atoms (upper bound) over one set of sites, which is ≈ 5.89 kJ/mol at the growth temperature (1023K). Therefore, one expects that it should be more difficult to realize SrO/ TiO_2 superlattices as compared to $\text{SrTiO}_3/\text{BaTiO}_3$ superlattice.

That the barriers to diffusion are low is somewhat unexpected. Based on the above-described results, the TiO_2 (SrO) migration rate through the SrO (TiO_2) block was rapid relative to the growth rate. Also, the process maintained the epitaxial nature of the perovskite film. In order for this to occur, the barrier must

be low and the mechanism must maintain the structural integrity of the growing film. The simplest conceivable mechanism is that Sr and Ti ions can coexist on (001) planes of the perovskite in considerable quantities for at least short periods of time, which would allow for the observed interdiffusion so long as the barriers were low. In the ideal perovskite, (001) planes are either SrO or TiO₂. In the Sr-rich regions, the Ruddlesden-Popper stacking faults observed in the Sr_{1+δ}TiO_{3+δ} and Sr₂TiO₄ films accommodate both the local non-stoichiometry and the structural coherency with the perovskite. It is known that the extra SrO plane (the stacking fault relative to the SrTiO₃ phase) can exist on the (100), (010), or (001) plane or longer-range disordered translation defects can occur, both of which lead to intermixing of the Sr and Ti cations on similar (001) planes.

On the Ti-rich side, mixed cationic occupancy of the (001) planes has not been observed previously. On the other hand, the diffraction pattern observed for the SrTi₂O₅ film (Fig. 4(c)) is best interpreted as having a perovskite structure with little difference in scattering power between the (001) planes. In other words, this diffraction pattern indicates that excess TiO₂ can be incorporated (at a level that was not determined and possibly only transient in nature) into SrTiO₃ structure in such a way to maintain the perovskite structure. One possible mechanism is that the SrTi₂O₅ film has some structural features common with BaTi₂O₅, the latter of which has planes that are derived from the (001) perovskite planes and that have mixed cationic character (with a complicated ordered structure that is not observed in our SrTi₂O₅ films). For such types of perovskite-derived structures that have intermixing of the Sr and Ti cations on (001) planes, one expects a loss of symmetry and a greatly diminished intensity in diffraction scans for the (001) and (003) perovskite peaks, as observed in our SrTi₂O₅ patterns. That TiO₂ incorporation does not occur for a slight Ti excess indicates that such incorporation is a higher energy mechanism than shifting the excess to interfaces and surfaces, and it likely does not occur until both of the lower energy mechanisms are saturated. More work is required to determine the precise structural incorporation mechanism in the SrTi₂O₅ film, but these XRD patterns argue that structural coherency can be maintained for Ti-rich phases having large deviations from the SrTiO₃ stoichiometry, a necessary requirement for the interdiffusion of SrO and TiO₂ layers.

Therefore, the fact that good quality, epitaxial SrTiO₃ films can be grown from ALD deposited blocks of SrO and TiO₂ that are each up to 33 monolayers thick can be summarized as follows. The free energy of formation of the compound from the oxides is large and provides a high driving force for compound formation. The fact that films with large excesses of both SrO and TiO₂ exhibit perovskite-related structures that are epitaxial with the substrate and coherent with the (001)-oriented SrTiO₃ structure indicates that interdiffusion is possible via local structural rearrangements, allowing for solid phase

epitaxial growth to occur in this system. Finally, the fact that the systems are observed to form good quality films indicates that the barriers to diffusion are small relative to the available thermal energy. It should be pointed out that decreasing the growth temperature led to a complete loss of crystallinity rather than the attainment of superlattice films, implying that ability of layers to crystallize are at least similar to their ability to interdiffuse.

The second point is that the value of m in the $(\text{SrO})_m(\text{TiO}_2)_m$ films plays a critical role in the relaxation behavior of the resultant SrTiO_3 films. For the SrTiO_3 ($m = 1$) films, the dislocation motion necessary for relaxation occurs entirely within the perovskite structure, resulting in partially strained films well beyond the critical thickness. For the block grown films (particularly for $m \geq 8$), relaxation of the SrO layers is immediate;²⁵ but this leads to a further excess of SrO in each monolayer beyond what is necessary for relaxed SrTiO_3 . The relaxation from this state to that of the final SrTiO_3 film, however, does not require classical dislocation motion; Sr cations are transported away from the interface during the reaction with the TiO_2 layers to form the fully reacted final film, which results in the necessary decrease in the SrO density in the SrO monolayers. Interestingly, this allows for the formation of extremely thin, relaxed, epitaxial SrTiO_3 films that may be of use as relaxed buffer layers to grow high quality perovskite films on dissimilar substrates. Furthermore the block-growth methods points to a solid-phase approach to attaining epitaxial films of compounds for which one of the components may be highly reactive with the substrate, such as SrTiO_3 on Si.

In summary, SrTiO_3 films with small and large global non-stoichiometries and local non-stoichiometries were grown by reactive molecular beam epitaxy using varied shuttering sequences (either ALD or MALD). It was observed by RHEED that the stoichiometry affected the surface reconstruction, with slight Sr excesses and small Ti excesses resulting in two-fold reconstructions along the $[110]$ and $[100]$ azimuths, respectively. Larger excesses - twice as much as required for SrTiO_3 growth - led to the formation of the Ruddlesden-Popper Sr_2TiO_4 phase for the Sr-rich film and a defective perovskite-like film for the Ti-rich film (SrTi_2O_5). Block layers of SrO and TiO_2 consisting of the same number of monolayers were deposited in an alternating fashion and interreacted completely to form highly crystalline SrTiO_3 (with single stacking-fault-like defects left at the original superperiod boundaries). The SrTiO_3 films grown in this manner were fully relaxed when the SrO and TiO_2 blocks were thicker than eight monolayers. Those with block thicknesses ranging between eight and ten monolayers were observed to have the narrowest FWHM values for the 2 θ peaks, even more narrow than the ALD SrTiO_3 films grown layer-by-layer ($m = 1$). The complete interreaction of the SrO and TiO_2 blocks to form epitaxial films is explained as a result of the large enthalpic driving force associated with the compound formation

and the observed ability of the perovskite structure in this system to tolerate large deviations from stoichiometry while maintaining structures coherent with (001)-oriented perovskites. The differences in film relaxation behavior between the alternating layer- and block-grown films is explained as resulting from the change in the growth mode.